Catalysis Science & Technology

Creation of Discrete Active Site Domains via Mesoporous Silica Poly(styrene) Composite Materials for Incompatible Acid-Base Cascade Reactions

Journal:	*Catalysis Science & Technology*
Manuscript ID	CY-ART-10-2020-001988.R1
Article Type:	Paper
Date Submitted by the Author:	22-Nov-2020
Complete List of Authors:	Cleveland, Jacob; Georgia Tech, Chemical and Biomolecular Engineering Kumar, Dharam; Georgia Institute of Technology, Schol of Chemical and Biomolecular Engineering Cho, Jinwon; Georgia Institute of Technology, e. School of Materials Science and Engineering Jang, Seung Soon; Georgia Institute of Technology, Materials Science and Engineering Jones, Christopher; Georgia Institute of Technology, Schol of Chemical and Biomolecular Engineering

Creation of Discrete Active Site Domains via Mesoporous Silica Poly(styrene) Composite Materials for Incompatible Acid-Base Cascade Reactions

Received 00th January 20xx,
Accepted 00th January 20xx

DOI: 10.1039/x0xx00000x

Jacob W. Cleveland,[a] Dharam Raj Kumar,[a] Jinwon Cho,[b] Seung Soon Jang,[b] and Christopher W. Jones*[a]

This work highlights the design and synthesis of bifunctional mesoporous silicate – polymer composite dual acid-base supported cascade catalysts. Compartmentalization of the two incompatible active sites is sought by segregating acid sites on the silica surface, and base sites within polymer chains and/or polymer domains. The ability to isolate and segregate active sites via control of the mesoporous silica pore size and polymer molecular weight is probed with silica samples functionalized by a grafting-to process. Supplemental activator and reducing agent (SARA) atom transfer radical polymerization is used to synthesize random copolymers containing protected primary amines. Thiol-ene 'click' chemistry facilitates silica functionalization via a convergent approach with the ene-functionalized polymer end group and silica-grafted thiols forming SBA/MCM-SH-poly(*styrene-co-2-(4-vinylbenzyl)isoindoline-1,3-dione*). Polymer deprotection and thiol oxidation produces primary amine / sulfonic acid containing composite catalysts. With the polymer supported Lewis base and silica grafted Brønsted acid, the two-step deacetalization – Knoevenagel condensation cascade is explored to assess the ability of these polymer/silica hybrids to segregate active sites, allowing both acid and base site accessibility. Six composite catalysts are synthesized and tested in individual and cascade reactions with kinetic results demonstrating that lower molecular weight SBA-15-P1 and MCM-41-P1 catalysts outperform (higher turnover frequencies and initial rates) their higher molecular weight analogues, as well as a polymer-free system containing molecular active sites dispersed on the silica surface. Higher molecular weight composite catalysts perform more poorly due to limited chain solubility, mass transfer limitations, and poor catalyst accessibility. In many cases, the polymer chains effectively thread into the mesopores, with higher moelcular weight polymers leading to pore blockage and inhibited mass transfer.

Introduction

Reaction cascades are processes where multiple synthetic transformations take place all in the same reaction vessel, sometimes also referred to as one-pot, domino, and tandem procedures.[1, 2] These processes often make use of multiple catalyst species and reaction pathways. Cascades have potentially large economic and environmental benefits by reducing waste-generating aspects of organic synthesis, such as offering a reduced solvent requirement, fewer purification steps, and also saving time.[3] In Nature, complex catalytic transformations occur rapidly in enzymes or clusters of enzymes producing the chemical species necessary for life. The efficiency of these systems results from primarily two distinct phenomena: (i) the partial or complete confinement of incompatible or opposing catalyst species in domains or compartments and (ii) the channeling of reaction intermediates from one site to the next.[4-6] While substrate channeling is a process that has yet to be demonstrated in synthetic systems, support of opposing molecular catalysts on the same support has been accomplished many times in literature, with systems based on organic polymeric supports,[7-15] functionalized mesoporous silicas,[16-23] zeolites,[24-26] metal-organic frameworks,[27-30] and Pickering emulsions.[31] In some cases, researchers have sought to compartmentalize different active sites in separate domains through the incorporation of a physical barrier such as use of distinct silica pores, incorporation into different blocks of polymeric backbones, and or in core-shell structures such as micelles.[13, 16, 32] Of course, for the purposes of chemical synthesis, one can always compartmentalize different sites in separate catalyst particles,[33-36] but this does not address the catalyst design issue of striving to develop single catalyst particles containing multiple types of segregated domains, as used in biological systems.

Compartmentalization is the concept in which catalyst design and particular synthetic routes are used to physically isolate species in distinct domains or regions. This idea is adapted from biological systems where many incompatible catalytic processes are occurring rapidly. Compartmentalization has only been accomplished thoroughly in a small number of non-biological works.[7, 9, 10, 16, 31, 37] The purpose of compartmentalization is to facilitate a reaction pathway that actively shields or segregates incompatible or opposing catalytic species, or their reagents, from one another, leading to physical isolation. A major benefit of these systems is that they can limit catalyst deactivation while potentially allowing for the environmental and economic benefits of eliminating some reaction and separation steps.

A variety of methods of compartmentalization have been reported over recent years. For example, shell-crosslinked micelles (SCM) compartmentalize orthogonal catalysts in the corona and shell of these systems.[7, 9, 32] In mesoporous SBA-15, acidic and basic functionalities have been separated in the mesopores and on the external surface of catalyst particles.[16, 38] In very few systems, researchers have combined the utility of both silica and polymer supported catalysis literature to create a combined system for

[a] School of Chemical & Biomolecular Engineering, Georgia Institute of Technology, 311 Ferst Dr., Atlanta, GA 30332-0100, United States
[b] School of Materials Science and Engineering, Georgia Institute of Technology, 771 Ferst Dr., Atlanta, GA 30332-0245, United States
† Footnotes relating to the title and/or authors should appear here.
Electronic Supplementary Information (ESI) available: See DOI: 10.1039/x0xx00000x

cascade catalysis.[22] The goal of this work is to create multi-domain catalyst particles combining the attributes of both silica and polymeric systems which could allow incorporation of an array of different types of active sites in the future. Silica domains can easily incorporate zones of controlled porosity, and silicates can incorporate active sites either within the silicate walls (e.g. by substitution of Si with Al, Fe, Ti, etc.) or via surface functionalization with organic, organometallic or metallic active sites. Polymeric structures can offer more dynamic domains, changing with external stimuli such as temperature, electric fields, or solvent changes, and active sites can be incorporated in the polymer's main chains or side chains.

In this work, we sought to expand the array of multi-domain catalyst particles by creating hybrid catalyst particles containing both silica mesopore and polymeric domains. As a demonstration of concept, we have deployed mesoporous SBA-15 and MCM-41 silica polymer composite materials as a platform to support incompatible molecular catalysts. These materials are synthesized via a grafting-to process using thiol-ene click chemistry. The efficacy of separation of silica supported Brønsted acids and polymer-bound Lewis bases is probed using varying polymer molecular weights and silica pore sizes. A classical reaction cascade, well-studied previously in other systems, comprising an acid catalyzed deacetalization followed by a base catalyzed Knoevenagel condensation is used as a test reaction sequence. This work thus attempts to demonstrate a generic method of establishing compartmentalization of incompatible chemical species in a mesoporous silicate – polymer composite system, allowing for further elaboration using the diversity of silica chemistry and polymer chemistry in the future.

Experimental

Materials, analytical tools and instrumentation, molecular dynamics simulation summary, synthesis of catalyst materials, catalyst synthesis and activation, control reactions and kinetic data and pore filling analyses are detailed in the Supporting Information.

Catalyst testing procedures

To probe the acid catalyst performance, the benzaldehyde dimethyl acetal deacetalization probe reaction is used. To a vial equipped with a magnetic stir bar, 0.25 mL of anhydrous MeCN and toluene is added (0.25 M). 20 µL of benzaldehyde dimethyl acetal, 10 µL of DI water (2 equiv), 10 mol% -SO_3H bifunctional catalyst, and 5 µL of decane is added. The vial is heated to 80 °C and the reaction progress is monitored via ^{1}H-NMR ($CDCl_3$) with timepoints using decane as an internal standard.

To probe the base catalyst performance, the Knoevenagel condensation of benzaldehyde with malononitrile is used. To a vial equipped with a magnetic stir bar, 0.25 mL of anhydrous MeCN and toluene is added (0.25 M). 13 µL of benzaldehyde dimethyl acetal, 10 mg of malononitrile (1.2 equiv), 5 mol% -NH_2 bifunctional catalyst, and 5 µL of decane is added. The vial is heated to 80 °C and the reaction progress is monitored via ^{1}H-NMR ($CDCl_3$) with timepoints using decane as an internal standard.

For the combined acid/base cascade procedure, a vial equipped with a magnetic stir bar, 0.25 mL of anhydrous MeCN and toluene is added (0.25 M). Then, 20 µL of benzaldehyde dimethyl acetal, 10 µL of DI water (2 equiv), 10 mg of malononitrile (1.2 equiv), 5 mol% -NH_2 bifunctional catalyst, and 5 µL of decane is added. The vial is heated to 80 °C and the reaction progress is monitored via ^{1}H-NMR ($CDCl_3$) with timepoints using decane as an internal standard.

Models and Simulation Methods

To investigate the dimension of poly(*st-co-NPhth*) chains in dichloromethane, fully atomistic simulation models are prepared to contain a single chain of poly(*st-co-NPhth*) with various molecular weights such as 3600, 6100, and 16000 g/mol, and 6400 dichloromethane molecules.

To describe the polymer-polymer and polymer-solvent interactions in molecular dynamics (MD) simulations, DREIDING force field is employed,[39] whose energy terms are

(1) $\boldsymbol{E_{total} = E_{vdW} + E_Q + E_{bond} + E_{angle} + E_{torsion} + E_{inversion}}$

where E_{tot}, E_{vdW}, E_Q, E_{bond}, E_{angle}, $E_{torsion}$ and $E_{inversion}$ are the total, van der Waals, electrostatic, bond stretching, angle bending, torsion, and inversion energies, respectively. E_Q is calculated from Mulliken charges which are obtained using density functional theory (DFT) with B3LYP functional and 6-31G** basis set.

After the initial structures are built using Monte Carlo techniques with three-dimensional periodic boundary conditions, annealing MD simulations are performed by changing the volume and temperature in order to accelerate the equilibration of the structures. Then, for data collection, equilibrium isobaric-isothermal ensemble (NPT) MD simulations are performed for 30 ns at 298.15 K and 1 atm. The equations of motion are integrated via the velocity Verlet algorithm[40] using a time step of 1.0 fs with Nose-Hoover thermostat.[41-43] For all of our MD simulations, we use the LAMMPS (Large-scale Atomic/Molecular Massively Parallel Simulator) software package.[44]

Results and Discussion

The main design hypothesis for this system was that polymer size and silica pore diameter can be used to control the 'click' location in the mesoporous particles and that this can lead to physical isolation of opposing catalysts. Specifically, we were interested in determining if primarily polymer pore filling, pore exclusion towards the mouth or external surface, or an intermediate of the two (Figure 1) could be achieved, leading to catalyst compartmentalization. It was hypothesized there are two distinct modes of catalyst compartmentalization that can take place in this system: (i) complete exclusion of the polymers from the pores via size control with the degree of polymerization and solvent choice (Case 1, core-shell) or (ii) cohabitation of both the grafted acid and polymer supported base domains inside the mesopores, confined in distinct 'pockets' of acids and bases created by the polymer network composite (Case 3, isolated pockets). Both methods have been shown to create efficient catalysts in separate systems in the literature, however the latter case has not for a silica-polymer composite catalyst but has for a porous, purely polymer system.[11, 13, 14, 16] The main tools used for the assessment of potential compartmentalization were the reaction kinetics, N_2 physisorption porosity analysis and a slate of control experiments. To determine whether polymer size has an impact on

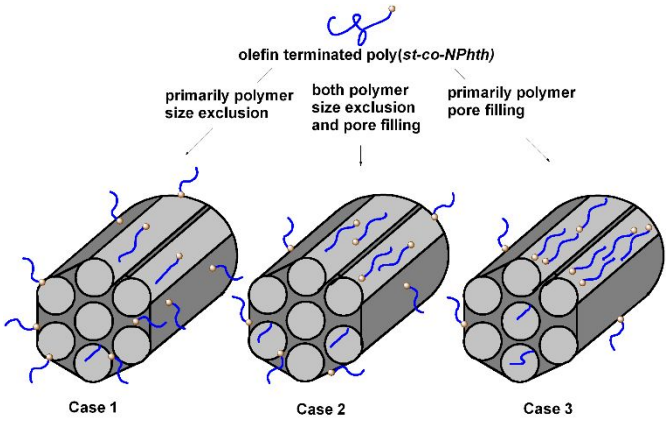

Figure 1. Illustration of the various polymer 'click' locations.

this phenomenon, a screening of molecular weights and silica pore diameters was conducted. To accompany this study, Table S1 highlights results from molecular dynamics simulations of the random copolymer used in this work at three separate molecular weights, yielding their radii of gyration (R_g) in the thiol-ene conditions, 25 °C and in DCM.

The overall functionalization route highlighted in Scheme 1 illustrates the four-step process for the synthesis of these acid-base bifunctional mesoporous silicate polymer catalysts. While it is noted that the grafting process will unselectively place thiols everywhere on the support, the majority will reside within the mesopores due to the large particle sizes used, which offer the majority of the surface area in the mesopores (see Figure S1 and S2). The Brønsted acid and Lewis base catalysts used in this system are a surface-grafted propylsulfonic acid and a polymer supported primary amine in the form of benzyl amine. These species are created from a surface-grafted thiol and phthalimide protected amine. First, either SBA-15 or MCM-41 (pore diameters of 7.0 and 2.4 nm, respectively) is functionalized with 3-mercaptopropy trimethoxy silane through grafting in dry toluene at 80 °C, forming SBA/MCM-SH (SBA/MCM-X; the slash is generic notation for materials made on both supports).[45]

Analysis of N_2 physisorption data and imaging of the bare SBA-15 and MCM-41 can be found in Figures S1, S2 and S3 in the supporting information. Next, the amine-containing terminal olefin end group polymers were subjected to the thiol-grafted support under thiol-ene click conditions, specifically with dimethoxyphenylacetophenone (DMPA), dichloromethane (DCM), and 365 nm ultraviolet (UV) light in a UV chamber.[46, 47] This forms SBA/MCM-SH-poly(*styrene-co-2-(4-vinylbenzyl)isoindoline-1,3-dione*) (referred to later as poly(*st-co-NPhth*). These are the main inactivated mesoporous silicate polymer composite precatalyst samples investigated in this study. The active, catalytic sites are created during deprotection of the polymer chains, with subsequent oxidation of remaining thiol groups to form sulfonic acids.

Random copolymers of styrene and 2-(4-vinylbenzyl)isoindoline-1,3-dione), referred to as poly(*st-co-NPhth*), were synthesized through supplemental activator and reducing agent atom transfer radical polymerizations[48, 49] (SARA-ATRP) using hex-5-en-1-yl 2-bromo-2-methylpropanoate (5-eneBMP) as the initiator.[46] These structures were analyzed via gel permeation chromatography (GPC) for molecular weight distributions and nuclear magnetic resonance (NMR) to confirm the copolymer structure and assess the structural integrity of the functional olefin end-group. Three molecular weights were synthesized for this study: poly(*st-co-NPhth*)-1, poly(*st-co-NPhth*)-2, poly(*st-co-NPhth*)-3 are M_n of 6100, 16000, and 45000 g/mol, with poly dispersities (Đ) of 1.16, 1.15, and 1.33, respectively. GPC traces, molecular weights, NMR end group analysis, and reactions conditions are all described Table S2 and Figure S5. SARA-ATRP was employed to generate controlled and narrow polymers with functional end-groups required for this study.

Next, two steps were deployed to generate the active acid and base sites required for the cascade reactions. First, the phthalimide protecting group was removed using aqueous hydrazine.[49]

Scheme 1. Functionalization route for the synthesis of the acid-base polymer composite catalysts

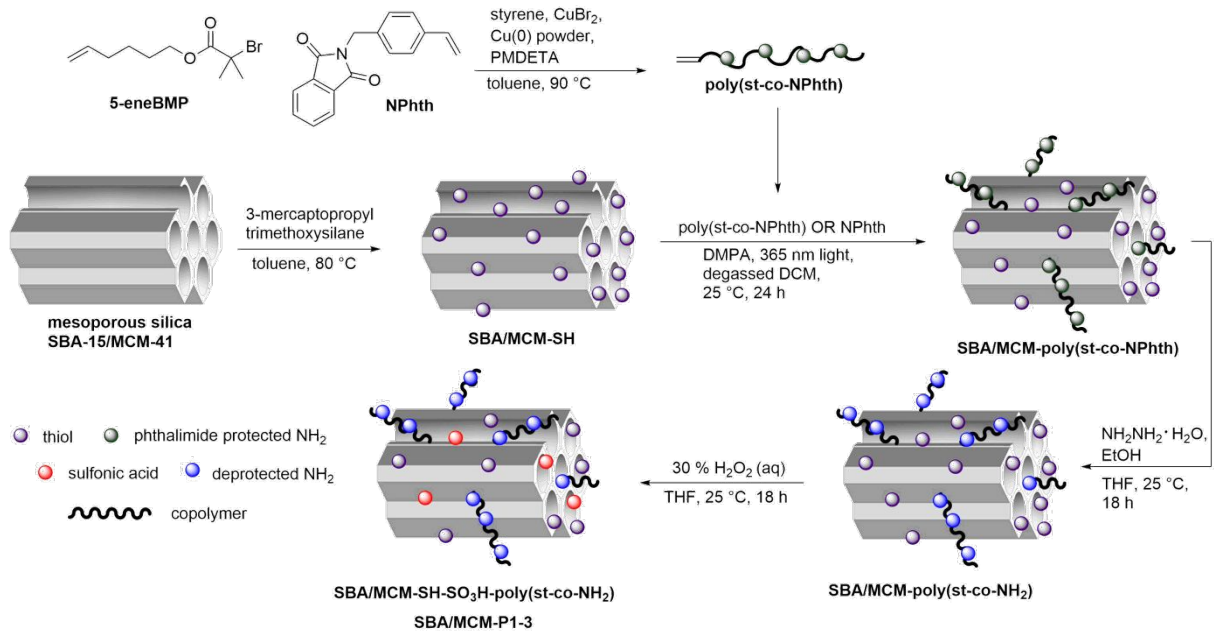

Table 1. Sample information of the mesoporous silicate composite and free NH_2 copolymer materials

Entry	Sample	Support	Polymer M_n[a] (g/mol)	Thiol[b] (mmol/g)	NH_2[b] (mmol/g)	SO_3H[c] (mmol/g)	SO_3H:NH_2
1	SBA-15-poly(*st-co-NPhth*)-1	SBA-15	6100	0.42	0.13	0.24	1.9
2	SBA-15-poly(*st-co-NPhth*)-2	SBA-15	16000	0.42	0.06	0.23	3.8
3	SBA-15-poly(*st-co-NPhth*)-3	SBA-15	45000	0.42	0.06	0.23	3.8
4	MCM-41-poly(*st-co-NPhth*)-1	MCM-41	6100	0.40	0.12	0.21	1.8
5	MCM-41-poly*(st-co-NPhth*)-2	MCM-41	16000	0.40	0.10	0.23	2.3
6	MCM-41-poly(*st-co-NPhth*)-3	MCM-41	45000	0.40	0.07	0.23	3.3
7	poly(*st-co-*NH_2)-1	-	5400	-	-	-	-
8	poly(*st-co-*NH_2)-2	-	15500	-	-	-	-
9	poly(*st-co-*NH_2)-3	-	43300	-	-	-	-
10	SBA-15-SO_3H-$PhCH_2NPhth$	SBA-15	-	0.42	0.14	0.26	1.9

[a] Determined by GPC using narrow poly(styrene) standards. [b] Determined through combustion CHN+S elemental analysis. [c]Determined after the deprotection and oxidation protocol through the back-titration method described in the supporting information

Overnight treatment was found to result in complete deprotection of the phthalimide, forming the primary benzyl amine species predicted to be active for the Knoevenagel condensation. Table 1 includes sample information regarding support and polymer combination with thiol, acid, and base loadings as well as SO_3H:NH_2 ratios. The base catalyst loading for each sample was determined through elemental analysis (EA). Lastly, the sulfonic acid was generated by oxidation of residual thiols on the surface of the mesoporous silicates that were left unreacted from the thiol-ene coupling.[50] Oxidation conditions were applied to the composite samples, and determination of the acid content by titrating the surface sulfonic acids using a NaCl solution as a ion exchanging agent.[16, 51, 52] Acid loadings are reported in Table 1 and were all found to be similar ~ 0.23 mmol/g. The detailed titration procedure is highlighted in the supporting information. From elemental analysis (EA), the parent SBA-15 and MCM-41 thiol functionalized samples contained 1.36% and 1.26% sulfur, respectively. The nitrogen content for the polymer containing samples was also assessed via CHN combustion analyses, and the N catalyst loadings were found to be between 0.06 and 0.13 mmol/g for all the catalyst samples. Thus, the catalyst samples generally had excess acid sites, relative to base sites.

From the simulation studies, the polymers of molecular weights of 3600, 6100, and 16000 g/mol were found to possess R_g in DCM at 25 °C of 0.92, 1.31, and 1.78 nm, respectively. The largest molecular weight copolymer synthesized for this study (45000 g/mol) was found to be too large for a full-atomistic simulation approach with explicit solvent molecules, thus, a lower 3600 g/mol polymer was included for comparison purposes on the low molecular weight end. When doubling the radii to obtain a diameter, it can be hypothesized that the lower molecular weight 6100 and 16000 g/mol copolymers (R_g of 1.31 and 1.78 nm) should be capable of fitting into the larger pore diameter SBA-15 silicate (7 nm pore diameter), while potentially

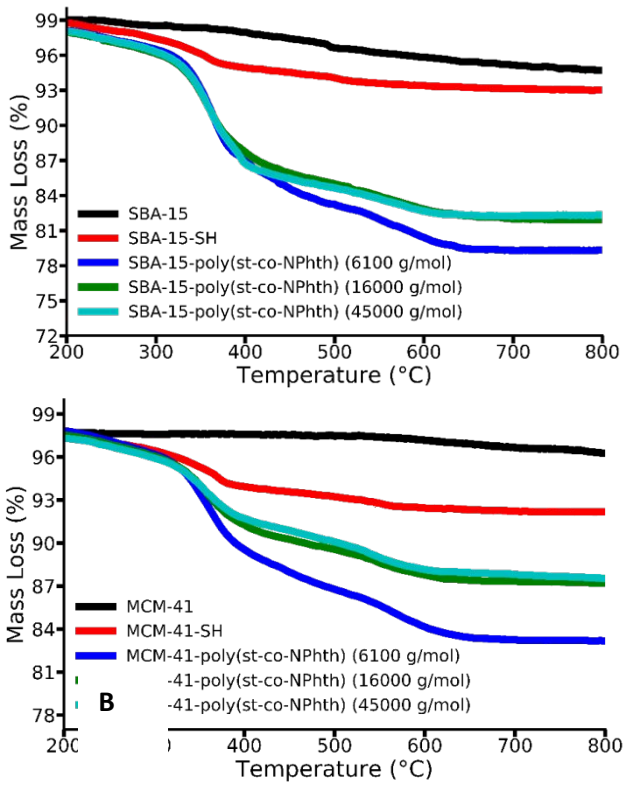

Figure 2. TGA curves for the bare silicates, thiol grafted, and polymer 'clicked' composite samples. Frame A highlights the SBA-15 functionalized samples where frame B is for the MCM-41 samples. These curves indicate the mass losses prior to deprotection and oxidation.

incurring resistance due to steric effects with the smaller pore MCM-41 (2.4 nm pore diameter). Even though simulation data at 45000 g/mol are not available, a similar statement could potentially be applied to the 45000 g/mol copolymer, with both inclusion and blocking occurring in SBA-15, with this polymer being totally excluded from the pores of MCM-41. However, it is noted that polymer morphology is a dynamic phenomenon in solution and that different conformations may occur, especially during the thiol-ene coupling reaction, which occurs in a different solvent.

The data in Table 1 describe several types of samples. SBA-15/MCM-41-poly(*st-co-NPhth*) refers to the protected and unoxidized materials. When these materials are deprotected and oxidized they are referred to as SBA-15/MCM-41- poly(*st-co-*NH_2)-X or SBA-15/MCM-41-PX, where X is a number from 1-3 denoting the polymer molecular weight deployed. Entries 1-3 in Table 1 refer to the SBA composite catalysts and entries 4-6 are for the MCM catalysts. Entries 7-9 are the free (untethered) deprotected (NH_2) catalysts that were used as a benchmark for the Knoevenagel condensation kinetics discussed later. Entry 10 is the analogous polymer-free bifunctional catalyst, containing grafted, molecular amine sites, synthesized for comparison purposes. For this sample, 2-(4-vinylbenzyl)isoindoline-1,3-dione) was directly coupled to the support via thiol-ene, then deprotected and oxidized.

Thermogravimetric analysis (TGA), elemental analysis, N_2 physisorption, and infrared (IR) spectroscopy were used to characterize the materials. TGA combustion analysis and N_2 physisorption data were cross compared to assess the total quantity of polymer functionalized on the thiol-grafted support, as well as to probe their physical location on the mesoporous silica particles (i.e. on the external surface/pore mouths or inside the pores). Figure 2 shows the TGA curves for bare supports, thiol-grafted, and click-functionalized samples used in this work. From the results, one can note that the total quantity of polymer attached to each of the SBA/MCM-poly(*st-co-NPhth*) samples on either silicate support is not equal (Table S3). This requires proper normalization procedures to assess important metrics, as discussed later. To this point, the thiol-ene coupling of polymer chains to each support material the total N:S ratio was held constant; however, the resulting polymer functionalized samples had some deviation in polymer content.

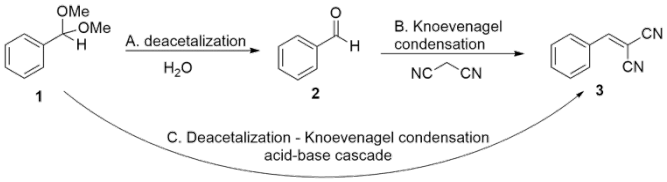

Figure 3. The probe acid-base reactions and cascade used to study the materials in this work.

Generally, the larger pore SBA-15 support allowed for incorporation of a higher weight percent of polymer than the smaller pore MCM-41, suggesting some polymer incorporation in the mesopore space, which is discussed further below. The SBA-15-poly(*st-co-NPhth*) composites contained 13-17 weight percent polymer, whereas for the MCM-poly(*st-co-NPhth*) samples, 6-12 weight percent polymer was observed. As a consequence of the varying polymer loadings between the SBA and MCM supports, the acid base ratios are slightly different, though in all cases the number of acid sites exceed the number of base sites (Table 1). For the low molecular weight (6100 g/mol) polymer samples, the SO_3H:NH_2 ratio is 1.9 and 1.8 for SBA-15 and MCM-41, respectively, whereas in the 16,000 and 45,000 g/mol samples for either silicate, the ratios are between two and four.

Table 2 reports the textural properties for the bare and functionalized supports used in this study. The pore sizes and BET surface areas for the bare SBA-15 and MCM-41 supports are 70 and 24 Å, and 730 and 1220 m^2/g_{SiO2}, respectively. After the thiol grafting process and thiol-ene experiments, the BET surface areas and pore volumes decrease significantly, as expected. When normalized to a common basis, the mass of silica in the sample, the BET surface area for the SBA-15 composite reduces from 623 m^2/g_{SiO2} for SBA-15-SH to 424 m^2/g_{SiO2} for SBA-15- poly(*st-co-NPhth*)-1. For the larger molecular weight composites, SBA-15-poly(*st-co-NPhth*)-2 and SBA-15-poly(*st-co-NPhth*)-3, the surface area is slightly higher at nearly 480 m^2/g_{SiO2} for each. For the MCM-41 composites, a less substantial difference in surface area was observed between MCM-41-SH and the MCM-41 composites, with a small drop from 1155 to 1025 m^2/g_{SiO2} for MCM-41-poly(*st-co-NPhth*)-1 and only 1047 and 1050 m^2/g_{SiO2} for MCM-41-poly(*st-co-NPhth*)-2 and MCM-41-poly(*st-co-NPhth*)-3. A similar trend in pore volume reduction can be seen for

Table 2. Textural properties for all bare and functionalized supports

Entry	Sample	D_p[a] (Å)	BET surface area[a] (m^2/g_{SiO2})	Pore volume[a] (cm^3/g_{SiO2})	ƒ (g_{pore}/g_{total})
1	SBA-15	70	730	0.93	-
2	SBA-15-SH	67	623	0.84	-
3	SBA-15-poly(*st-co-NPhth*)-1	61	424	0.66	0.91
4	SBA-15-poly(*st-co-NPhth*)-2	63	481	0.70	0.86
5	SBA-15-poly(*st-co-NPhth*)-3	63	479	0.71	0.85
6	MCM-41	24	1220	0.82	-
7	MCM-41-SH	23	1155	0.68	-
8	MCM-41-poly(*st-co-NPhth*)-1	21	1025	0.59	0.83
9	MCM-41-poly(*st-co-NPhth*)-2	22	1047	0.65	0.70
10	MCM-41-poly(*st-co-NPhth*)-3	22	1050	0.66	0.70
11	SBA-15-SO_3H-$PhCH_2NPhth$	66	483	0.68	-

[a] D_p: Pore diameter, [a] Determined through N_2 physisorption analysis at 77 K; See Figure S7, S8, and S9 for thiol-graft silicate and composite isotherms as well as raw N_2 physisorption BET areas and pore volumes.

these samples as well. The lowest pore volumes were observed for each system with SBA-15- poly(*st-co-NPhth*)-1 and MCM-41- poly(*st-co-NPhth*)-1, having the shortest polymer chains, at 0.66 and 0.59 cm^3/g_{SiO2}, respectively. Using normalized pore volumes before and after the thiol-ene reaction, the polymer filling fraction (g_{pore}/g_{total}), which estimates the mass of polymer inside the pores relative to the total polymer mass (from TGA), one can gain insight into how much of the polymers reside inside the mesopores versus how much are on the external surface or pore mouths (See supplemental, equation 1). These estimates suggest that for the SBA-15 composites, over 85% of the polymer mass resides inside the pores. This is likely a consequence of the large pore diameter of the parent silica of 70 Å. Surprisingly, we also calculate relatively high polymer pore fractions for the MCM-41 composites, despite the smaller pores of MCM-41. These were estimated to be 0.83, 0.70 and 0.70 for MCM-41-poly(*st-co-NPhth*)-1, 2, and 3, respectively. Comparing these fractions with the illustration of the various cases in Figure 1, it appears that none of the systems can be accurately labeled as case 1, where there is primarily polymer pore exclusion. The SBA-15-poly(*st-co-NPhth*)-1, 2, 3, and MCM-41-poly(*st-co-NPhth*)-1 composites can be thought of as primarily polymer pore filling (case 3), while MCM-41-poly(*st-co-NPhth*)-2 and 3 appear to be more pore filling than exclusion but more of a mixed system between case 1 and 3, with fractions at 0.70 for both (case 2). When comparing these results to the predictions based on the simulation data, it appears that polymer R_g is not an effective tool to predict polymer tethering location and ultimately pore filling in these systems. A very limited control of pore filling and exclusion seems to be acquired with these polymers and silica. Perhaps a greater degree of control can be found using polymers of significantly higher molecular weight and silicas or zeolites of smaller pore diameters. These data reflect similar results reported in the literature regarding the very few examples of threading of polymers into mesoporous structures.[53, 54] In our work, instead of physically mixing the silica and polymer, the thiol-ene coupling, which covalently tethers the polymers to a particular thiol on the support, restricts its motion to some degree, and prevents removal via the washing treatments. This work is the first report, to our knowledge, of tethering/threading polymers into mesoporous silicas for the purposes of cascade reactions.

FT-IR spectroscopy was used to confirm the presence and then the deprotection of the phthalimide protected amines on the NPhth units in the polymer chains on the composites (Figure S13). The presence of the carbonyl group from the phthalimide protected amine was confirmed by the C=O stretching at 1700 cm^{-1}. Upon deprotection in aqueous hydrazine, the IR spectra indicate a loss in signal in this region (Figure S13). A smaller mass loss from 200-700 °C in thermogravimetric analysis compared to the protected samples also indicated removal of the bulky phthalimide group (Figure S14).

After full characterization of the composite materials, kinetic analyses were performed to assess the efficacy of the catalysts, as well as to rationalize the structural data. As mentioned above, the cascade reaction used in this study is the acid catalyzed deacetalization of benzaldehyde dimethyl acetal followed by the base catalyzed Knoevenagel condensation with malononitrile to form benzylidene malononitrile, with benzaldehyde as the intermediate (Figure 3). Reaction conditions were a 0.25 M cosolvent solution of a 1:1 v:v mixture of MeCN and toluene at 80 °C. For reaction A, 2 molar equiv. of water was used. For reaction B, 1.2 equiv. of malononitrile was used and for reaction C, water and malononitrile were both used. Similar to a previous report, reaction kinetics for just the deacetalization (using benzaldehyde dimethyl acetal and no malononitrile) and the Knoevenagel condensation (using benzaldehyde as a starting material and no water) were used to probe the efficacy of these dual acid-base bifunctional catalysts for the purposes of assessment of Lewis base and Brønsted acid performance, or more broadly, to gauge the likelihood of active site compartmentalization occuring.[11] These data were gathered to understand the nature of the polymer domains and their interaction with the remainder of the composites and if the polymer molecular weight or silica pore diameter impact the catalytic behavior. All reactions were normalized using 5 mol% nitrogen (or 10 mol% acid in reactions probing the acid kinetics, since SO_3H:NH_2 ratios vary) and turnover frequencies (TOFs) and initial rates of reaction were calculated from the approximately linear low conversion/time regime, typically the first 30 minutes. Base site TOFs were normalized by total amine catalyst present in the sample using N content from elemental analysis. TOFs for the acid kinetics were normalized by total acid content determined from the aforementioned titration method.

Table 3. Initial rates and TOFs for reactions A and B separately with the synthesized catalyst samples

Several control experiments were performed to better understand the catalytic results obtained with the new bifunctional catalysts (Table S4). The background activity of both reactions using

Entry	Catalyst	Initial rate (M/h)[a]	TOF (10^{-3} s^{-1})[a]	Initial rate (M/h)[b]	TOF (10^{-3} s^{-1})[b]	SO_3H:NH_2
1	SBA-15-SO_3H-$PhCH_2NH_2$	0.72	15.4	0.08	1.7	1.9
2	SBA-15-P1	0.18	4.0	0.43	9.5	1.9
3	SBA-15-P2	0.42	9.3	0.14	3.1	3.8
4	SBA-15-P3	0.69	15.3	0.05	1.1	3.8
5	MCM-41-P1	0.24	5.3	0.40	8.9	1.8
6	MCM-41-P2	0.84	18.6	0.01	0.2	2.3
7	MCM-41-P3	1.29	28.6	0.01	0.2	3.3
8	poly(*st-co-NH_2*)-1	-	-	1.19	25.2	-
9	poly(*st-co-NH_2*)-2	-	-	0.99	21.0	-
10	poly(*st-co-NH_2*)-3	-	-	0.70	14.7	-

[a] Determined from reaction A, [b] Determined from reaction B

no catalysts (entry 1 and 2) was low, with 10% and 6% conversion in 6 h for reactions A and B, respectively. The unoxidized thiol supported sample was also tested and showed catalytic activity (SBA-15-SH, entry 4, reaction A). Two samples were prepared that possess one out of the two potential active centers, SBA-15-SO_3H-poly(*st-co-NPhth*) and SBA-15-SH-poly(*st-co-*NH_2); see Figure S15 for the synthesis routes. Both catalysts were tested using the cascade reaction C (Table S5, entries 1 and 2) and the monofunctional acid catalyst SBA-15-SO_3H-poly(*st-co-NPhth*) showed near complete conversion to intermediate 2 while 0% conversion to 3. SBA-15-SH-poly(*st-co-*NH_2) showed minimal conversion to 2 with 8% conversion, while yielding only 2% to cascade product 3.

Another important control experiment is the test of the polymer-free dual acid-base bifunctional catalyst SBA-15-SO_3H-$PhCH_2NH_2$ (Table 2, entry 11. Table 3, entry 1). This sample was prepared by direct thiol-ene coupling of the 2-(4-vinylbenzyl)isoindoline-1,3-dione monomer to SBA-15-SH, followed by the same deprotection and oxidation procedures. The initial rate for reaction B with this material (Table 3, entry 1) was 0.08 M/h, which is considerably lower than the best performing free copolymer poly(*st-co-*NH_2) and best performing composites, SBA-15-P1 and MCM-41-P1.

Figure 4 (frame A and B) shows the kinetic profiles for the Knoevenagel condensation reaction (reaction B) performed with all six of the SBA-15-P1-3 and MCM-41-P1-3 catalysts. It can be noted from the SBA-15 kinetics that activity decreased as the polymer molecular weight increased, similarly to the kinetics with the deprotected free amine copolymer catalysts (Figures S10 and S11). A noticeable drop in the initial rate was observed as the degree of polymerization increased for these untethered, silica-free catalysts. This is generally a well understood trend in polymer supported catalysis, arising from diffusional limitations using larger polymer sizes, though it does not rule out other factors in the composite system, such as differing polymer chain solubility inside the pores or other pore effects such as polymer swelling constraints due to confinement.[55-57] Entries 8-10 in Table 3 show the initial rates and for the silica-free polymer samples, poly(*st-co-*NH_2)-1-3, being 1.19, 0.99, and 0.70 M/h with polymers of 5400, 15500, and 43300 g/mol, respectively. In the large pore SBA-15 composite samples (entries 2-4), a moderate drop in the initial rate for reaction B was observed as the polymer size increased, with 0.43, 0.14, and 0.05 M/h observed over SBA-15-P1, P2, and P3, respectively. With the MCM-41 composites also in reaction B (entries 5-7), kinetic experiments indicate a nearly identical initial rate using MCM-41-P1 compared to SBA-15-P1, at 0.4 M/h; however, with the larger polymer chains in the MCM composites, significant losses in activity were observed, with very small initial rates of 0.01 M/h for both samples These results rival background reactivity at around 6% conversion to 3 in 6 h. Figure 5 shows a graphical bar chart illustrating the difference in the composite catalysts using the metrics of TOFs based on initial rates.

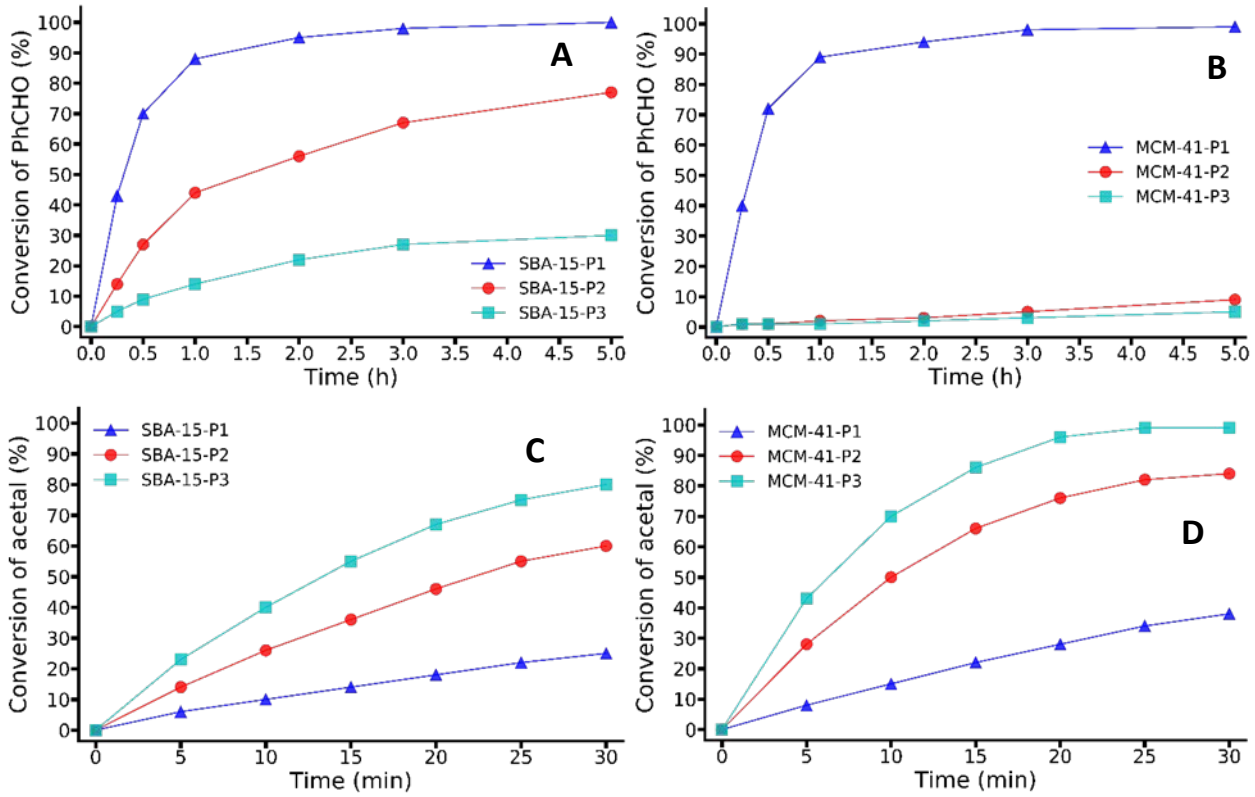

Figure 4. Kinetic profiles for the base catalyzed Knoevenagel condensation (reaction B) using the SBA-15 and MCM-41 bifunctional composite catalysts (frame A and B). Kinetic profiles for the acid catalyzed deacetalization (reaction A) using the SBA-15 and MCM-41 bifunctional composite catalysts (frame C and D). Conversion was monitored by ^{1}H-NMR using decane as an internal standard.

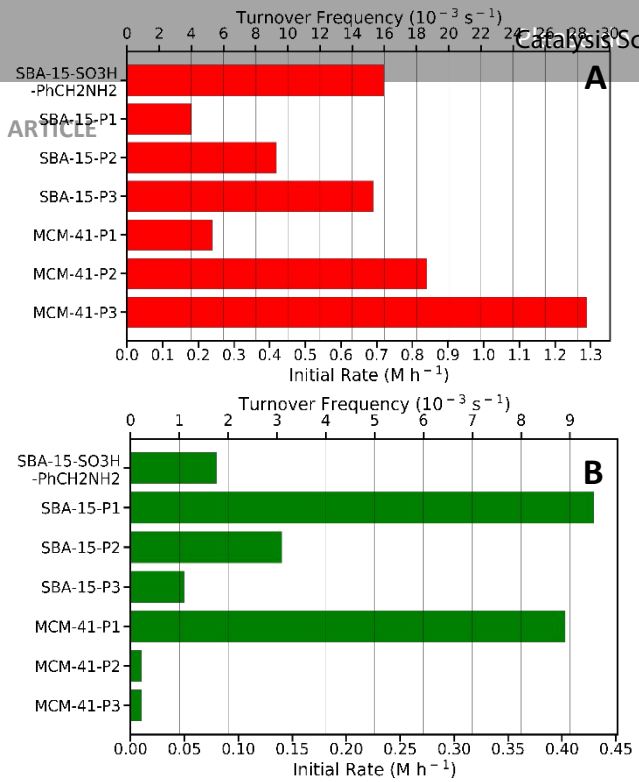

Figure 5. Bar chart representations of the initial rates and TOFs for all bifunctional silica catalyst samples during only reaction A (frame A) and only reaction B (frame B). corrected figure

Figure 4 (frame C and D) shows solely the acid catalyzed deacetalization kinetics (using benzaldehyde dimethyl acetal as a starting material and no malononitrile, reaction A) using the SBA-15 (frame C) and MCM-41 (frame D) composite catalysts. It can be qualitatively seen based on the curves that the performance for reaction A follows the opposite trend observed for the Knoevenagel condensation, with the samples that showed the lowest activity in the Knoevenagel condensation showing the highest activity in the deacetalization reaction. In contrast to the performance of these catalysts in reaction B, where initial rates decreased with an increase in polymer size, the initial rates for reaction A in the SBA-15 and MCM-41 composites increased with increasing polymer length, being 0.18, 0.42, and 0.69 M/h for SBA-15-P1, P2, and P3, respectively. This trend was more clearly evident with the MCM-41 composites, with rates of 0.24, 0.84, and 1.29 M/h for P1, P2 and P3.

Seeking catalysts that possessed significant bifunctionality, offering good rates in each reaction step, SBA-15-P1 and MCM-41-P1 were selected and employed in the full reaction cascade (reaction C) as shown in Figure 6 (SBA-15-P1). These catalysts were also recycled by centrifuging and decanting the liquid for several cycles (entries 5-7 in Table S6), showing modest reusability with a conversion of 1 at 90% after the third cycle at the same timepoint of 7 h. SBA-15-SO_3H-$PhCH_2NH_2$ was also employed in reaction C (Figure S16) and showed considerably lower activity. The initial rates for formation of cascade product (3) during reaction C (full reaction cascade) shows 0.1 M/h for both SBA-15-P1 and MCM-41-P1 with 0.04 M/h for SBA-15-SO_3H-$PhCH_2NH_2$. This is likely due to the poor performance in the second cascade step (perhaps from acid/base quenching) which is evident by a large build-up of the intermediate 2 (PhCHO) with a slow rate of formation of 3.

Despite the complexity of this system, we can propose several factors to rationalize the results obtained. The observed reduction in TOF of the free, unsupported amine copolymers (poly(*st-co-*NH_2)-1-3) (Table 3, entries 8-10) supports a baseline understanding of why the composite catalyst systems perform more poorly with higher molecular weight polymers; however, the severity of the loss in performance requires additional consideration. When comparing the TOFs for the SBA-15-SO_3H-$PhCH_2NH_2$, SBA-15-P1, and MCM-41-P1 in reaction B, the TOF of 1.7×10^{-3} s^{-1} for the polymer-free system is much lower compared to the relatively high TOF of 9.5×10^{-3} s^{-1} with SBA-15-P1 (and similarly high MCM-41-P1 at 8.9×10^{-3} s^{-1}) during the standalone Knoevenagel condensation. Especially when comparing the nearly identical SO_3H:NH_2 ratio for these three systems, one can infer that the polymer plays a more complex and subtle role than simply acting as a support for the Lewis base active sites. Noting that the pore filling fraction for SBA-15-P1 (SBA-15-poly(*st-co-NPhth*)-1) was 0.91 (0.83 for MCM-41-P1), one may categorize these samples as a case 3 system (Figure 1). The fact that such a system, where the polymer is wholly or mostly contained within the mesopore, yields an effective catalyst suggests that some acid and base sites are freely available, and that acids and bases may be cohabitating the same porous structure but still maintaining physical separation through means of spacing. The spacing could be associated with acid and base sites in different pore channels, or because portions of the channels contain "pockets" of incompatible active sites that "shield" each other in a single pore.

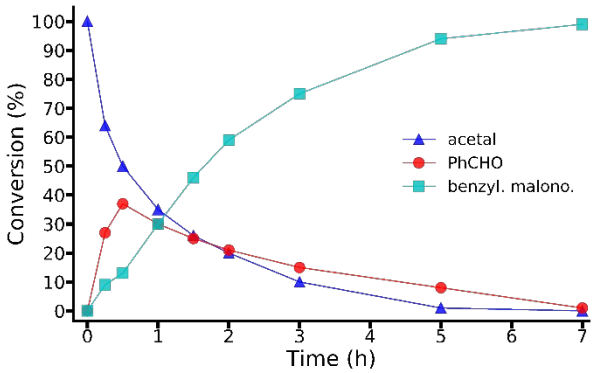

Figure 6. Full kinetic profile of reaction C with the SBA-15-P1 brush catalyst. Quantification of **1**, **2**, and **3** was determined from ^{1}H-NMR using decane as an internal standard.

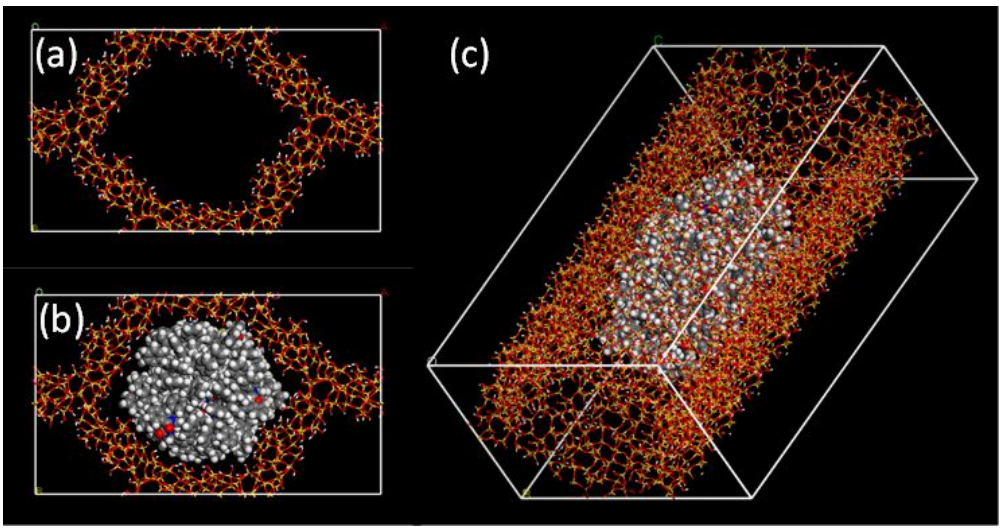

Figure 7. Front view (a) of the 16,000 g/mol poly(*st-co-NPhth*) *MCM*-41 model; Front view (b) and tilted view (c) of 16,000 g/mol poly(*st-co-NPhth*) included in MCM-41 pore. White: H, gray: C, red: O, blue: N, orange: Si.

When comparing just the SBA-15 composite samples, we can note a steady decrease in TOF of the amine catalysts (reaction B) as the polymer molecular weight increases, with 9.5×10^{-3} s^{-1} for SBA-15-P1 and 3.1×10^{-3} and 1.1×10^{-3} s^{-1} for P2 and P3. In an opposite fashion, the TOFs for the acid catalysts (reaction A) increase as a function of polymer size with an uptick from 4.0×10^{-3} in SBA-15-P1 to 9.3×10^{-3} and 15.3×10^{-3} in P2 and P3. SBA-15-P1 shows the best activity in both reactions while for the larger polymer SBA-15-P2 and P3, these show more dominant performance in reaction A compared to reaction B. The acid to base ratios for these samples are nearly 2 for P1 and 4 for P2 and P3. The increase in the ratio could potentially be responsible for the lack in performance for the higher molecular weight SBA-15 composites in reaction B, resulting from contact between thee amine and sulfonic acid sites leading to deactivation. However, this is contrary to the previous suggestion that in the presence of polymer, active sites become nested inside "pockets" inside the mesopores, thus mitigating quenching. Another point of consideration is that the larger polymers inside the mesopores could also be creating zones of inaccessible or poorly utilized amine sites resulting from a dense crowding and/or poor solubilizing/swelling of polymers.

A similar, but more pronounced trend can be found with the MCM-41 composite catalysts with a remarkable drop in TOF of the amine sites (reaction B) as a function of polymer molecular weight with 8.9×10^{-3} s^{-1} for MCM-41-P1 and 0.2×10^{-3} and 0.2×10^{-3} s^{-1} for P2 and P3. And similarly with the SBA case above, a drastic increase in acid TOF (reaction A) with molecular weight can be found at 5.3×10^{-3} in MCM-41-P1 to 18.6×10^{-3} and 28.6×10^{-3} in P2 and P3. In these systems, the SO_3H:NH_2 ratio is nearly 2 for P1 and 2 and 3 for P2 and P3, noting these are lower in comparison to the SBA-15 composites (for MCM-41-P2 and P3); however, we see a complete loss in catalytic activity for the higher molecular weight MCM-41 composites. These results could represent complete quenching of amine sites or more likely, total blocking of some of the pores due to the narrow pore structure during the reaction while the polymers are partially solvated. With the large polymers in such narrow pores, there could possibly still exist "pockets" of active acid and base sites, however, if they exist the data suggest they are largely inaccessible to the acetal and benzaldehyde starting materials for their respective reactions.

After building a representative polymer composite system with a 16,000 g/mol poly(*st-co-NPhth*) in the pores of MCM-41 (Figure 7) at 25 °C and no solvent, one can notice observe a significant degree of polymer confinement and pore congestion, potentially resulting in mass transfer limitations. This conveys why the higher molecular composite MCM-41 systems exhibit a large loss in activity for the Knoevenagel condensation reaction, if this moderate length polymer is highly constrained. Another important note is that the reactions are performed at a much higher temperature than the temperature that the molecular dynamics simulations were conducted (80 ^{o} C vs 25 ^{o} C). The MD analysis was conducted under the thiol-ene temperature conditions to model the radii of gyration of the polymers during the coupling reaction. At the significantly higher temperature where the reaction kinetics were studied, and in the presence of solvent molecules the polymer size due to swelling will be larger than at room temperature. Thus, an increase in polymer swelling at an elevated temperature could further hinder pore diffusion of reactant molecules and accessibility of active sites.

At high composite molecular weight (16,000 g/mol and higher) base activity is considerably lower than that of the small 6,100 g/mol polymers in both SBA-15 and MCM-41 supports. These data suggest that smaller polymer sizes are more capable of providing access to both acid and base sites in an efficient manner. As noted before, a few previous works isolated incompatible acid and base catalyst solely within porous polymeric structures.[11, 13] In this case, potentially a similar phenomenon is occurring within the mesopores of these silicates. The drop-off in TOF for SBA-15-P3 with 1.1×10^{-3} s^{-1} or 0.2×10^{-3} s^{-1} in MCM-41-P2 and P3 for reaction B suggests that the longer or larger the size of the polymer domains impacts active site accessibility, perhaps due to poor solvation and swelling of the polymer,[55-57] catalyst quenching between the adjacent acid sites, and mass transfer limitations to Lewis base active sites. Since the acid to base ratio in both SBA-15-P2 and P3 is close to 4 (and 2.2 and 3.3 for MCM-41-P2 and P3, respectively), this helps provide some rationalization of why the acid catalyzed reaction proceeds quickly while the base catalyzed reaction begins to slow if the issue is catalyst quenching. In addition, TOFs fall from 8.9×10^{-3} s^{-1} in MCM-41-P1 to 0.2×10^{-3} s^{-1} for both MCM-41-P2 and P3 in reaction B. Such a sharp drop in activity indicates a near total loss of catalysis occurring,

resulting from catalyst inaccessibility or active site quenching, or a synergy of the two effects in these systems. Inaccessibility may partly result from a 'mushroom' polymer morphology effectively burying the Lewis bases inside a poorly solubilized collapsed polymer composite due to the low grafting density.[58-60] This effect gives reason as to why the external surface tethered polymers in MCM-41-P2 and P3 (30% of total polymers) still poorly participate in reaction B.

Conclusion

In summary, this work demonstrates a previously unexplored route for incorporating Brønsted acidic and Lewis basic molecular functionalities onto a mesoporous support. A particular focus was placed on segregating active sites in polymer and silica domains in a single particle, akin to how biological systems segregate active sites in different particles or organelles. Using MD simulations in the thiol-ene conditions (25 °C, DCM) gave insight in how degree of polymerization effects radii of gyration. Targeting polymer brush domains on the external surface of mesoporous silica supports, to our surprise, the polymer chains primarily threaded themselves into the silica mesopores. This implies the design element of using MD simulations to inform whether degree of polymerization could be used as tool to size exclude polymers from the mesopores ultimately proved to show little effect.

Thiol-ene coupling was used to link SARA-ATRP derived protected amine polymers to the thiol-loaded silica surface, yielding polymer-silica hybrid particles. By using polymers of varied molecular weight and silica materials with different pore sizes, we sought to use size exclusion to prevent large molecular weight Lewis base bearing polymers from 'clicking' inside the pores, where the majority of Brønsted acids reside. In an alternate hypothesis, we also considered that cohabitation of both the grafted acid and polymer-supported base inside the pores could function effectively if they were separated by space inside the mesopores by the silica walls or inert poly(styrene) backbones in the polymer.

Rates in the individual reactions were used to assess the efficacy of the catalysts or more specifically, to determine which of the 6 composite samples contained the most significant bifunctionality towards each reaction. The highest initial rate found for reaction A and the lowest initial rate found for reaction B are from MCM-41-P3 with 1.29 and 0.01 M/h, respectively. Meanwhile, the highest initial rate found for reaction B and lowest initial rate found for reaction A are from SBA-15-P1 with 0.43 and 0.18 M/h, respectively. It was determined that in the composites where reaction A exhibited the strongest performance, reaction B suffered significantly, often showing little to no catalytic activity (SBA-15-P3, MCM-41-P2, MCM-41-P3). On the other hand, the composites where reaction B performed the strongest, reaction A suffers but much less when compared to the previous case (SBA-15-P1, SBA-15-P2, and MCM-41-P1). Therefore, the catalysts showing the most significant degree of bifunctionality were SBA-15-P1, SBA-15-P2, and MCM-41-P1. When comparing the SBA-15-P1 and MCM-41-P1 composite catalysts with the polymer-free bifunctional catalyst, SBA-15-SO_3H-$PhCH_2NH_2$, both the polymer catalysts significantly outperform the polymer-free system in reaction B but underperform in reaction A. These results potentially indicate that the polymers are playing a larger role in compartmentalization rather than just as a support for the Lewis base catalysts.

The largest TOF of 9.5 s^{-1} found from this work (SBA-15-P1, reaction B) shows a modest improvement in comparison to other systems in literature.[11] This approach ultimately produced a bifunctional catalysts system capable of cohabitation of grafted Brønsted acid and polymer supported Lewis base active sites inside the pores of mesoporous silica. Future research in the group will focus on new methods to create compartmentalization in porous-oxide systems with acids and bases and other types of incompatible molecular catalysts.

Conflicts of interest

There are no conflicts to declare.

Acknowledgements

We gratefully thank the U.S. Department of Energy, Office of Basic Energy Sciences Catalysis Science Contract DEFG02-03ER15459 as the funding source for this work. Ryoh-Suke Sekieya is acknowledged for the assistance in synthesizing the catalysts for this study.

Notes and references

1. L. F. Tietze and U. Beifuss, *Angewandte Chemie International Edition in English*, 1993, **32**, 131-163.
2. I. Wheeldon, S. D. Minteer, S. Banta, S. C. Barton, P. Atanassov and M. Sigman, *Nature Chemistry*, 2016, **8**, 299.
3. R. A. Sheldon, *Green Chemistry*, 2007, **9**, 1273-1283.
4. S. Tsitkov and H. Hess, *ACS Catalysis*, 2019, **9**, 2432-2439.
5. A. Kuzmak, S. Carmali, E. von Lieres, A. J. Russell and S. Kondrat, *Scientific Reports*, 2019, **9**, 455.
6. Y. R. Yang, J. Fu, S. Wootten, X. Qi, M. Liu, H. Yan and Y. Liu, *ChemBioChem*, 2018, **19**, 212-216.
7. P. Qu, M. Kuepfert, S. Jockusch and M. Weck, *ACS Catalysis*, 2019, **9**, 2701-2706.
8. L. F. Xiong, H. Zhang, Z. D. He, T. Q. Wang, Y. Xu, M. H. Zhou and K. Huang, *New Journal of Chemistry*, 2018, **42**, 1368-1372.
9. M. Kuepfert, A. E. Cohen, O. Cullen and M. Weck, *Chemistry – A European Journal*, 2018, **24**, 18648-18652.
10. L. C. Lee, J. Lu, M. Weck and C. W. Jones, *Acs Catalysis*, 2016, **6**, 784-787.
11. E. Merino, E. Verde-Sesto, E. M. Maya, M. Iglesias, F. Sanchez and A. Corma, *Chemistry of Materials*, 2013, **25**, 981-988.
12. E. Verde-Sesto, E. Merino, E. Rangel-Rangel, A. Corma, M. Iglesias and F. Sanchez, *Acs Sustainable Chemistry & Engineering*, 2016, **4**, 1078-1084.
13. X. Wang, L. Zhang, Z. Guo, Y. Shi, Y. Zhou and J. Wang, *Applied Surface Science*, 2019, **478**, 221-229.
14. Z. Sun, X. Yang, X. Huang, M. Zhang, G. Bian, Y. Qi, X. Yang and W. Zhang, *New Journal of Chemistry*, 2019, **43**, 16676-16684.
15. K. W. Wang, Z. F. Jia, X. K. Yang, L. Wang, Y. L. Gu and B. E. Tan, *Journal of Catalysis*, 2017, **348**, 168-176.
16. Z. H. Weng, T. Y. Yu and F. Zaera, *Acs Catalysis*, 2018, **8**, 2870-2879.
17. D. C. Zhang, J. Y. Xu, Q. K. Zhao, T. Y. Cheng and G. H. Liu, *Chemcatchem*, 2014, **6**, 2998-3003.
18. F. P. Shang, J. R. Sun, H. Liu, C. H. Wang, J. Q. Guan and Q. B. Kan, *Materials Research Bulletin*, 2012, **47**, 801-806.

19. S. Shylesh and W. R. Thiel, *Chemcatchem*, 2011, **3**, 278-287.
20. F. Zhang, G. H. Liu, W. H. He, H. Yin, X. S. Yang, H. Li, J. Zhu, H. X. Li and Y. F. Lu, *Advanced Functional Materials*, 2008, **18**, 3590-3597.
21. J. Meng, F. Chang, Y. Su, R. Liu, T. Cheng and G. Liu, *ACS Catalysis*, 2019, **9**, 8693-8701.
22. M. Gao, F. Chang, S. Wang, Z. Liu, Z. Zhao and G. Liu, *Journal of Catalysis*, 2019, **376**, 191-197.
23. R. H. Jin, D. S. Zheng, R. Liu and G. H. Liu, *Chemcatchem*, 2018, **10**, 1739-1752.
24. R. J. Kalbasi, S. Mansouri and O. Mazaheri, *Research on Chemical Intermediates*, 2018, **44**, 3279-3291.
25. B. Hernandez, J. Iglesias, G. Morales, M. Paniagua, C. Lopez-Aguado, J. L. G. Fierro, P. Wolf, I. Hermans and J. A. Melero, *Green Chemistry*, 2016, **18**, 5777-5781.
26. B. Y. Liu, C. Wattanaprayoon, S. C. Oh, L. Emdadi and D. X. Liu, *Chemistry of Materials*, 2015, **27**, 1479-1487.
27. L. Feng, Y. Wang, S. Yuan, K.-Y. Wang, J. Li, G. S. Day, D. Qiu, L. Cheng, W.-M. Chen, S. Madrahimov and H.-C. Zhou, *ACS Catalysis*, 2019, DOI: 10.1021/acscatal.8b04960.
28. W. L. Jiang, Q. J. Fu, B. J. Yao, L. G. Ding, C. X. Liu and Y. B. Dong, *Acs Applied Materials & Interfaces*, 2017, **9**, 36438-36446.
29. B. Y. Li, D. X. Ma, Y. Li, Y. M. Zhang, G. H. Li, Z. Shi, S. H. Feng, M. J. Zaworotko and S. Q. Ma, *Chemistry of Materials*, 2016, **28**, 4781-4786.
30. Y. Zhang, Y. X. Wang, L. Liu, N. Wei, M. L. Gao, D. Zhao and Z. B. Han, *Inorganic Chemistry*, 2018, **57**, 2193-2198.
31. H. Q. Yang, L. M. Fu, L. J. Wei, J. F. Liang and B. P. Binks, *Journal of the American Chemical Society*, 2015, **137**, 1362-1371.
32. J. Lu, J. Dimroth and M. Weck, *Journal of the American Chemical Society*, 2015, **137**, 12984-12989.
33. N. T. S. Phan, C. S. Gill, J. V. Nguyen, Z. J. Zhang and C. W. Jones, *Angewandte Chemie International Edition*, 2006, **45**, 2209-2212.
34. B. Helms, S. J. Guillaudeu, Y. Xie, M. McMurdo, C. J. Hawker and J. M. J. Frechet, *Angewandte Chemie-International Edition*, 2005, **44**, 6384-6387.
35. Y. G. Chi, S. T. Scroggins and J. M. J. Frechet, *Journal of the American Chemical Society*, 2008, **130**, 6322-+.
36. Y. L. Huang, B. G. Trewyn, H. T. Chen and V. S. Y. Lin, *New Journal of Chemistry*, 2008, **32**, 1311-1313.
37. C. C. Zuo, W. J. Wei, Q. Zhou, S. P. Wu and S. J. Li, *Chemistryselect*, 2017, **2**, 6149-6153.
1 38. Y. Huang, S. Xu and V. S.-Y. Lin, *Angewandte Chemie International Edition*, 2011, **50**, 661-664.
39. S. L. Mayo, B. D. Olafson and W. A. Goddard, *The Journal of Physical Chemistry*, 1990, **94**, 8897-8909.
40. W. C. Swope, H. C. Andersen, P. H. Berens and K. R. Wilson, *Journal of Chemical Physics*, 1982, **76**, 637-649.
41. S. Nose and M. L. Klein, *Journal of Chemical Physics*, 1983, **78**, 6928-6939.
42. S. Nose, *Journal of Chemical Physics*, 1984, **81**, 511-519.
43. S. Nose, *Mol Phys*, 1984, **52**, 255-268.
44. S. Plimpton, *J Comput Phys*, 1995, **117**, 1-19.
45. C. von Baeckmann, R. Guillet-Nicolas, D. Renfer, H. Kählig and F. Kleitz, *ACS Omega*, 2018, **3**, 17496-17510.
46. T. B. Mai, T. N. Tran, M. Rafiqul Islam, J. M. Park and K. T. Lim, *Journal of Materials Science*, 2014, **49**, 1519-1526.
47. A. B. Lowe, *Polymer Chemistry*, 2010, **1**, 17-36.
48. R. Whitfield, A. Anastasaki, V. Nikolaou, G. R. Jones, N. G. Engelis, E. H. Discekici, C. Fleischmann, J. Willenbacher, C. J. Hawker and D. M. Haddleton, *Journal of the American Chemical Society*, 2017, **139**, 1003-1010.
49. S. M. Gravano, M. Borden, T. von Werne, E. M. Doerffler, G. Salazar, A. Chen, E. Kisak, J. A. Zasadzinski, T. E. Patten and M. L. Longo, *Langmuir*, 2002, **18**, 1938-1941.
50. E. Cano-Serrano, G. Blanco-Brieva, J. M. Campos-Martin and J. L. G. Fierro, *Langmuir*, 2003, **19**, 7621-7627.
51. Y. Noda, K. Li, A. M. Engler, W. A. Elliott and R. M. Rioux, *Catalysis Science & Technology*, 2016, **6**, 5961-5971.
52. R. S. Li, H.; Chen, J., *Catalysts* 2018, **8**.
53. H. L. Frisch and J. E. Mark, *Chemistry of Materials*, 1996, **8**, 1735-1738.
54. N. T. Vo, A. K. Patra and D. Kim, *Physical Chemistry Chemical Physics*, 2017, **19**, 1937-1944.
55. M. Benaglia, A. Puglisi and F. Cozzi, *Chemical Reviews*, 2003, **103**, 3401-3430.
56. P. H. Toy and K. D. Janda, *Accounts of Chemical Research*, 2000, **33**, 546-554.
57. T. J. Dickerson, N. N. Reed and K. D. Janda, *Chemical Reviews*, 2002, **102**, 3325-3344.
58. S. Yamamoto, M. Ejaz, Y. Tsujii and T. Fukuda, *Macromolecules*, 2000, **33**, 5608-5612.
59. S. Turgman-Cohen and J. Genzer, *Macromolecules*, 2010, **43**, 9567-9577.
60. M. Asai, D. Zhao and S. K. Kumar, *ACS Nano*, 2017, **11**, 7028-7035.

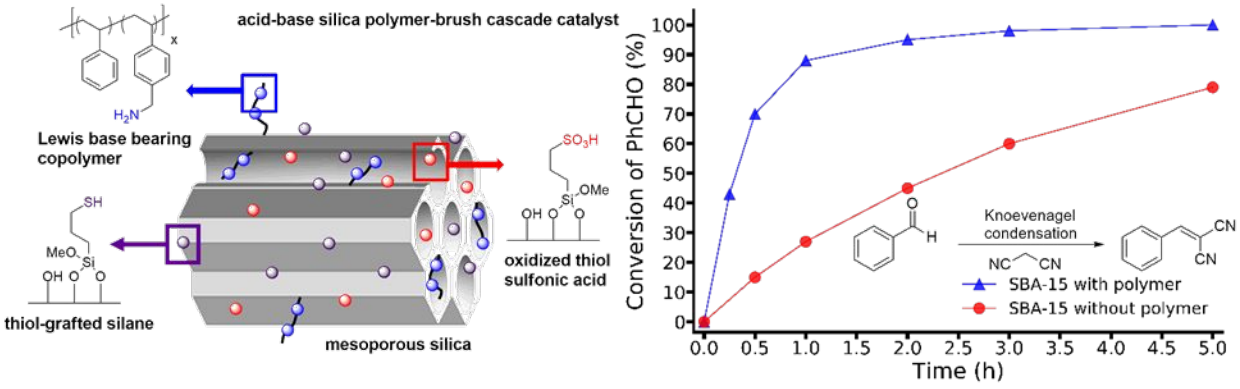

Mesoporous silica polymer composite materials successfully catalyze a two-step acid and base cascade reaction. Research emphasizes compartmentalization of incompatible Lewis base and Bronsted acid catalysts tuning polymer chain length and silica pore diameter.